Engineering Structures 213 (2020) 110581

Contents lists available at ScienceDirect

Engineering Structures

journal homepage: www.elsevier.com/locate/engstruct

Damage assessment of GFRP bar reinforced ultra-high-strength concrete beams under overloading impact conditions

Zein Saleh[a], M. Neaz Sheikh[a,*], Alex Remennikov[a], Abheek Basu[b]

[a] School of Civil, Mining and Environmental Engineering, University of Wollongong, Australia
[b] Gravitas Technologies Pty Ltd., Port Kembla, NSW 2505, Australia

ARTICLE INFO

Keywords:
Damage assessment
GFRP
Impact
Reinforced concrete beams
Shear capacity
Ultra-high-strength concrete

ABSTRACT

This paper investigates the damage assessment of Glass Fiber Reinforced Polymer (GFRP) bar reinforced Ultra-High Strength Concrete (UHSC) beams under overloading impact conditions. The overloading impact condition is defined as the input impact energy larger than the quasi-static energy absorption capacity of the beam. Impact (drop load) tests were carried out on nine GFRP bar reinforced UHSC (GFRP-UHSC) beams. Three increasing input impact energies were used in this study. To investigate the influence of the shear capacity on the damage of the GFRP-UHSC beams, the beams were designed with three different shear capacities. The midspan deflection histories, dynamic forces, and accelerations along the beams were measured. The crack patterns were recorded using a high-speed video camera to analyze the failure modes of the beams. It was found that the shear reinforcement ratio, longitudinal reinforcement ratio, and input impact energy influenced the failure modes of the GFRP-UHSC beams under overloading impact conditions. Flexural and flexural-shear failure modes were observed in beams with higher shear capacities, whereas dominant shear and flexural-shear failure modes were observed in beams with lower shear capacities. Design recommendations for GFRP-UHSC beams to resist overloading impact conditions are provided.

1. Introduction

During the last few decades, Glass Fiber Reinforced Polymer (GFRP) bars have emerged as suitable replacements for steel bars in Reinforced Concrete (RC) structures. GFRP bars are anisotropic, have high strength-to-weight ratio, do not corrode, have higher ultimate strengths than steel bars, and are non-electromagnetic. Therefore, GFRP bar reinforced concrete structures are the most suitable in aggressive and corrosive environments. The flexural behavior and shear behavior of GFRP bar reinforced concrete beams under monotonic loads were investigated extensively in the literature in the last two decades [1–13]. The bond characteristics of GFRP bars were also thoroughly investigated in the literature [14–20]. The range of the compressive strengths of concrete investigated was between Normal Strength Concrete (NSC) of 20 MPa and High Strength Concrete (HSC) of 80 MPa. However, a few studies investigated the behavior of GFRP bar reinforced concrete beams with concrete strengths higher than 80 MPa [21]. In this study, the concrete having a compressive strength higher than 100 MPa was considered ultra-high-strength concrete (UHSC) [22].

The use of HSC and UHSC beams especially in bridges and high-rise buildings is becoming more popular due to the superior strength and stiffness of HSC and USHC over-normal-strength concrete. Recently, GFRP bar reinforced HSC (GFRP-HSC) beams have been gaining popularity. The flexural behavior of GFRP-HSC beams was extensively investigated in the literature and was found to be superior to the flexural behavior of the GFRP bar reinforced NSC (GFRP-NSC) beams [7,23–26]. To ensure ductility, the design codes [27,28] recommend concrete failure before FRP bar rupture since it is a less severe failure mode. This provides some ductility before the failure of the beams. However, the behavior of UHSC beams is different from that of NSC beams due to the brittleness of the UHSC and the lower ductility of the UHSC beams. It was reported in the literature that brittle shear failure occurs in HSC and UHSC beams [29–33]. The relatively smooth and trans-angular cracks in HSC, along with the absence of interlocking of the aggregate particles in HSC, reduce the contribution of aggregates to the shear strength of the beam. This leads to the brittle shear failure of HSC beams.

During the last few decades, RC structures around the world have been increasingly subjected to impact loads caused by events including terrorist attacks, vehicle accidents, and natural disasters. Impact loads cause catastrophic failure of the structures. Therefore, it is important to

* Corresponding author.
E-mail address: msheikh@uow.edu.au (M.N. Sheikh).

https://doi.org/10.1016/j.engstruct.2020.110581
Received 8 August 2019; Received in revised form 22 February 2020; Accepted 26 March 2020
Available online 06 April 2020

design the structures against impact loads. It is noted that the response of GFRP bar reinforced concrete beams under monotonic loads is different from the response of GFRP bar reinforced concrete beams under low-velocity impact loads.

A few studies investigated the behavior of GFRP-NSC and GFRP-HSC beams under input impact energies equivalent to the quasi-static Energy absorption capacity (E) of the beam [10,34]. However, the beams did not completely fail and showed signs of reserve capacities. It was reported that the failure input impact energy was higher than its quasi-static Energy absorption capacity (E). Therefore, overloading impact conditions were used in this study to assess the damage and the reserve capacity of the beam. Overloading impact is defined as the input impact energy higher than E.

Several studies in the literature investigated the impact response of beams strengthened with FRP [35,36]. However, the shear behavior of GFRP bar reinforced concrete beams under low-velocity impact loads has not been adequately investigated [10,37–39]. It was reported in Saleh et al. [40] that the shear capacity of the GFRP-RC beams has a significant influence on the behavior of the beams under overloading impact conditions. However, no study has yet investigated the effect of the shear capacities of GFRP-UHSC beams under overloading impact conditions.

This study explores, through experimental investigations, the damage of GFRP-UHSC beams under overloading impact conditions. The low-velocity impact loads tests were carried out using the high-capacity impact testing facility at the University of Wollongong. The influences of the shear capacities and impact energies were discussed. This study provides a detailed assessment of the damage of GFRP-UHSC beams under overloading impact conditions. Moreover, design recommendations for GFRP-UHSC beams under impact loads were proposed. It is noted that investigation on the influence of the span-to-depth ratio on the behavior of GFRP-UHSC under overloading impact conditions is considered beyond the scope of this study.

2. Experimental program

2.1. Material properties

To determine the compressive strength of concrete, nine 150 mm × 300 mm cylinder samples were cast on the day of concrete casting. The target compressive strength of concrete at 28 days was 80 MPa. Three cylinders were tested after 28 days of concrete casting, on the first day of impact load tests (day 126), and on the last day of impact load tests (day 138). The MATEST Servo-Plus Evolution machine was used for the testing of the compressive strengths of concrete. The average compressive strength of concrete at 28 days was 97.6 MPa. However, the average compressive strength of concrete on the first and last day of impact load tests was 118 MPa. Therefore, the compressive strength of concrete of the beams was reported as 118 MPa in this study.

To determine the tensile properties of the GFRP bars, eight GFRP bars were tested to determine the average modulus of elasticity and ultimate strength of the GFRP bars. The tensile tests were carried out using the INSTRON machine. The tensile stress-strain curves of the eight tested GFRP bars are presented in Fig. 1. It can be observed from Fig. 1 that all GFRP bars showed linear behavior until the rupture of the bars. The average modulus of elasticity of the GFRP bars was 44 GPa and the average ultimate tensile strength of the GFRP bars was 966 MPa.

2.2. Details of the GFRP-UHSC beams

In total, nine GFRP-UHSC beams were tested in this study under low-velocity impact loads. In addition, one GFRP-UHSC beam was tested under quasi-static loads as a control beam to determine the Energy absorption capacity (E) of the control beam. All the GFRP-UHSC beams were 200 mm in width, 300 mm in depth, and 2400 mm in length. The clear span of the beams was 2000 mm. The clear concrete cover was 25 mm at the top, bottom, and the sides of the beams. All the beams were reinforced with GFRP longitudinal bars and GFRP transverse shear bars. The longitudinal bars comprised two 16 mm GFRP bars placed in tension and two 16 mm GFRP bars placed in compression. Table 1 presents the details of the tested beams. The GFRP-UHSC beams were designed as over-reinforced according to ACI [27], considering the target compressive strength of concrete of 80 MPa. Due to the large difference between the target compressive strength of concrete and the achieved compressive strength of concrete during the impact test period (target = 80 MPa and achieved = 118 MPa), the beams were under-reinforced according to ACI [27]. The shear reinforcement calculations were carried out according to ACI [27] and CSA [28]. The shear reinforcement comprised 12 mm GFRP bars. The spacing of the shear reinforcement was varied so that the GFRP-UHSC beams achieved three different shear capacities. The maximum allowed spacing between the GFRP stirrups as per the recommendations of ACI [27] and CSA [28] was taken into account. The spacings of the GFRP stirrups were 150 mm, 100 mm, and 75 mm corresponding to $D/2$, $D/3$, and $D/4$, respectively, where D is the depth of the beam. The details of the beams were presented in Fig. 2. The variables of this study were the shear capacity of the beams and the impact energies.

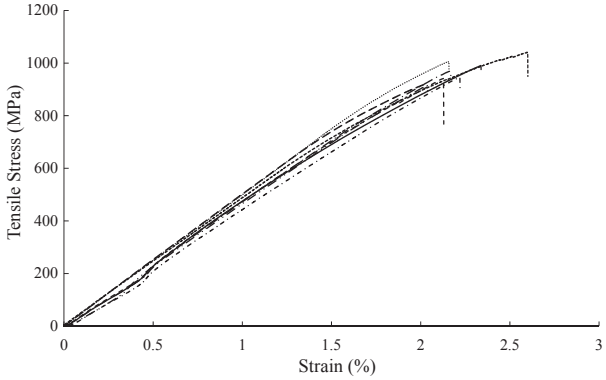

Fig. 1. Tensile stress-strain curves of the 16 mm diameter GFRP bars.

2.3. Experimental program

One control beam was tested under quasi-static three-point bending loading to determine the load-midspan deflection response of this control beam. The control beam had the same properties as the beams tested under impact loads. The control beam was tested under quasi-static loads (displacement controlled) at the rate of 1 mm/min. The load was applied onto a steel plate placed on top of the control beam at its midspan. The applied load was recorded using a load cell and the midspan deflection was recorded using ACUITY AR550-250 laser displacement transducer placed below the midspan of the control beam. Since the control beam was under-reinforced (considering the achieved compressive strength of concrete during impact loads testing), the predicted failure mode was GFRP bar rupture. The quasi-static Energy absorption capacity (E) of the control beam was calculated as the area under the load-midspan deflection curve [9,12,41,42]. The impact velocities were then chosen for this experiment based on E as 5.5 m/s, 6 m/s, and 6.5 m/s. The choice of the impact velocities is explained in detail in Section 3.1.

Nine GFRP-UHSC beams were tested under low-velocity impact loads using the high capacity impact test machine at the University of Wollongong. The test setup for the impact load tests was shown in Fig. 3. The supports of the beams were placed at a distance of 200 mm from both edges of the beam. A pin and a roller support were used. The impact hammer was restricted to the vertical motion only. The total

Table 1
Details of the tested GFRP-UHSC beams.

Beam group	Beam Name	Dimensions of Beam (mm)	Compressive strength of concrete (MPa)	Longitudinal reinforcement (mm)	Reinforcement ratio (ρ)(%)	Ratio of reinforcement ρ/ρ_b	Transverse reinforcement	
							Bar diameter (mm)	Spacing (mm)
1	150-5.5	200 (Width)	118	Two 16 mm bars	0.76	0.97	12	150
	100-5.5			(Tension)				100
	75-5.5	300 (Depth)						75
2	150-6			Two 16 mm bars				150
	100-6	2400 (Length)		(Compression)				100
	75-6							75
3	150-6.5							150
	100-6.5							100
	75-6.5							75
Control beam	Control beam							100

mass of the impact hammer was 600 kg. The impactor was flat, made of steel, and had a diameter of 300 mm. The impact hammer was released from a height (h), where h is the drop height. The drop height was determined by using the equilibrium of kinetic energy and potential energy ($mgh = 0.5mv^2$), where m is the mass of the impact hammer, g is the gravitational acceleration, and v is the impact velocity.

The nine beams tested under impact loads were divided into three groups to investigate the influence of the shear capacities of the beams on the damage of the beams under overloading impact conditions. Each group contained three beams with the spacing of $D/2$ (or 150 mm), $D/3$ (or 100 mm), and $D/4$ (or 75 mm). Groups 1, 2, and 3 were subjected to impact velocities of 5.5 m/s, 6 m/s, and 6.5 m/s, respectively. A MEMRECAM HX-7 high-speed video camera was used to record the tests at 5000 frames/sec. A 5 mm rubber pad was placed on the top of the beam at the impact zone to protect the concrete from crushing. Two reaction frames were used to prevent the uplift of the beam after impact (Fig. 3). The impact load was measured using a high-capacity load cell connected to the impact hammer. The duration of the impact was measured as 60 ms from the instance the impactor hit the beam until the beam returned to its initial position. The reaction forces were measured using load cells placed below the supports of the beams. Six accelerometers were mounted to one side of the beam to measure the acceleration of the beam during the first few milliseconds to analyze the inertia effects. All experimental data were recorded at a sampling rate of 100 kHz. Square grids with 50 mm sides were drawn on one face of the GFRP-UHSC beams to help in tracking the cracks. The beams were labelled by two numbers, the first number indicates the spacing of the shear reinforcement and the second number indicates the impact velocity. For example, Beam 75-6 indicates that the beam with a stirrup spacing of 75 mm and was tested under an impact velocity of 6 m/s.

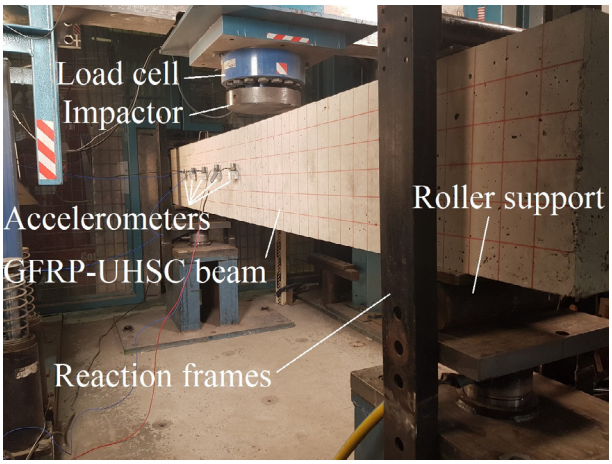

Fig. 3. Drop-weight impact loads test set-up.

3. Experimental results and discussion

3.1. Quasi-static loads test

Three-point bending load test was carried out on the GFRP-UHSC control beam to measure its quasi-static Energy absorption capacity (E). The control beam was similar in dimensions to the nine beams tested under impact loads. The supports placed below the beam were roller and pin supports. The deflection controlled (displacement controlled) quasi-static loads were applied at a rate of 1 mm/min at the midspan of the control beam. The load was applied until the failure of the beam. The control beam failed by tensile GFRP bar rupture. This was

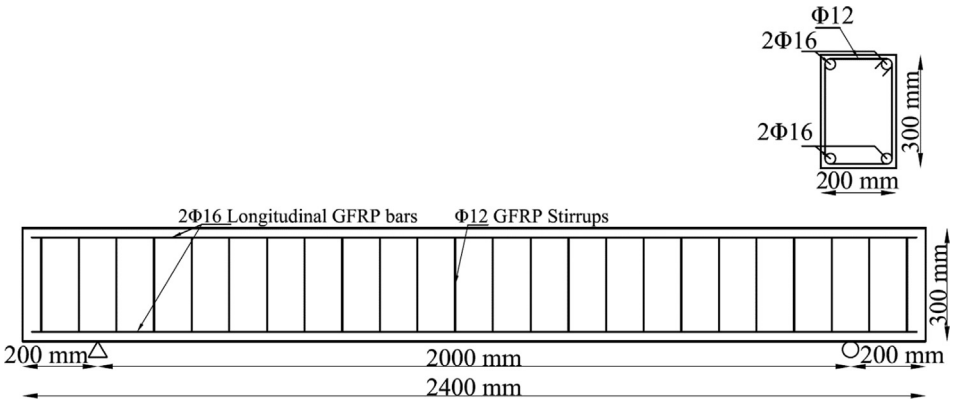

Fig. 2. Details of the GFRP-UHSC beams tested.

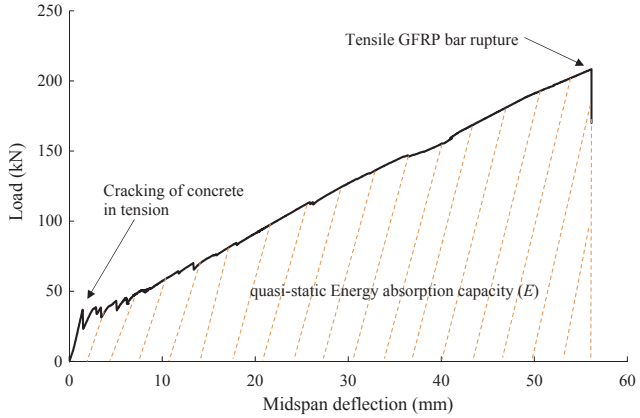

Fig. 4. Load-midspan deflection response of the control beam specimen.

consistent with an under-reinforced failure of a GFRP-UHSC beam [37]. The load-midspan deflection response is presented in Fig. 4. The load-midspan deflection response of the control beam was bilinear up till failure. The experimental cracking load was 35.6 kN. After the cracking of the concrete, the stiffness of the beam reduced. Flexural cracks were observed in the beam. The load increased until it reached approximately 200 kN when partial rupture of GFRP bars started taking place. The load increased until the ultimate capacity of 208 kN was attained when the GFRP bars fully ruptured. The midspan deflection corresponding to the ultimate load was 56.1 mm. The quasi-ductile behavior due to cracking of concrete in compression [10,37] was not observed before failure. The failure of the control beam was sudden due to the rupture of the GFRP bars. The concrete in compression was almost intact. The energy absorption capacity (E) of the control beam was calculated as the area under the load-midspan deflection curve (Fig. 4.). The value of E of the control beam was 6.6 kJ. Then, E was equated to the input impact energy ($\frac{1}{2}mv^2$) of the drop hammer to determine the input impact velocity for the impact load tests [10,34]. In order to investigate the damage of the GFRP-UHSC under overloading impact conditions, impact energies higher than E of the control beam were applied. It was reported in Goldston et al. [10] that GFRP-NSC and GFRP-HSC small-scale beams tested under low-velocity impact loads did not fail when subjected to an input impact energy of value E. Therefore, input impact energies of 1.4E, 1.6E, and 1.8E were applied in this study to assess the damage of GFRP-UHSC beams under overloading impact conditions. The three impact velocities applied on the three groups of beams were 5.5 m/s, 6 m/s, and 6.5 m/s. The nine beams tested under impact loads had different shear capacities. All nine beams were compared to the control beam with a stirrups spacing of 100 mm. When the shear capacity of a GFRP-UHSC beam increases, the E of the beam increases as well [5]. However, the increase in the E was not significant and it was considered acceptable to assume in this study that the E of all nine beams was similar.

In order to quantify the damage of the beams, the beams that were subjected to overloading impact conditions were also tested under quasi-static loads after impact to determine their residual load-carrying capacities. In this study, the residual load-carrying capacity (residual capacity hereafter) of the beam (P_r) is defined as the load-carrying capacity of that beam after being subjected to impact loads. The residual capacity of the beam (P_r) was then compared to the load-carrying capacity of the control beam (208 kN). The residual capacities of the beams would indicate the level of damage of each beam after impact loads.

Based on the experimental observations, three levels of damage of GFRP-UHSC beams were considered in this study: (i) Minor when P_r was over 90%, (ii) Medium when P_r was between 80% and 90%, and (iii) Severe when P_r was under 80%.

3.2. Dynamic equilibrium of applied forces

The forces present during an impact are the reaction force, inertia load, and impact load. When the impactor strikes the beam, the beam accelerates downwards in the direction of the motion of the impactor. The impact load is resisted by the stiffness of the beam while the beam accelerates downwards. The acceleration of the beam creates the inertia load which acts opposite to the direction of motion of the beam. The impact load, at any instant, equals the sum of the inertia load and the reaction force [43]. The inertia load of the beam is calculated as the integral of the mass per unit length of the beam multiplied by the acceleration of the beam over its length as shown in Eq. (1):

$$\int_0^L \bar{m}\ddot{u}(x,t)dx + R(t) = I(t) \tag{1}$$

where L is the length of the beam, $\bar{m}$ is the mass per unit length of the beam, $\ddot{u}$ is the acceleration of a particular point on the beam, R is the total reaction force, and I is the impact load.

The impact load in this experiment was recorded using a load cell connected to the impactor. The reaction forces were recorded using load cells placed below the supports. The accelerations were recorded using accelerometers attached externally to the front side of the beam, as shown in Fig. 5. The accelerometers were attached only to one side of the beam and symmetry was assumed for the other side. The accelerometers were spaced at 200 mm. The change in the acceleration between two adjacent accelerometers was assumed linear. The impact load, reaction forces, and inertia load are presented in Fig. 5.

Fig. 6 presents the dynamic equilibrium of the applied force history for Beam 75-6 for the duration of impact. The impact load started from zero and increased until it reached a maximum force of 620 kN at

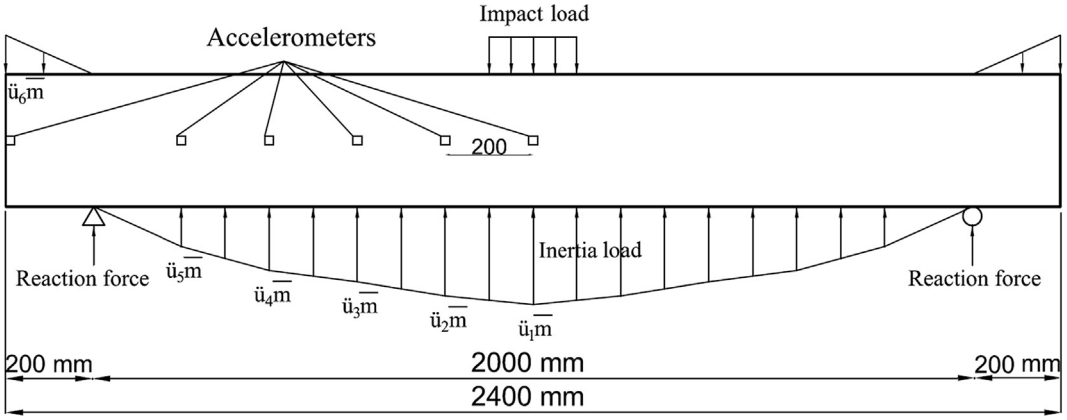

Fig. 5. Distribution of dynamic loads along the beam.

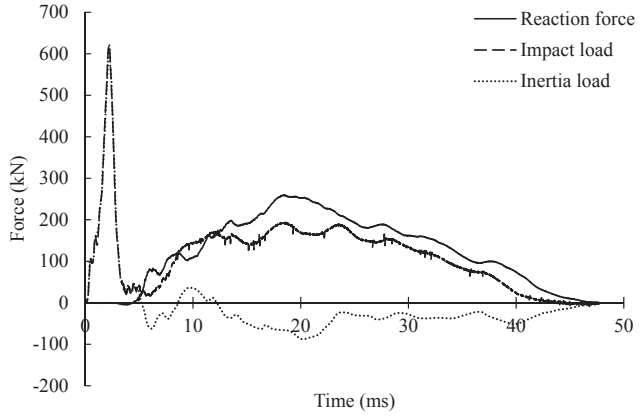

Fig. 6. Dynamic equilibrium of applied forces for Beam I-75-6.

1.7 ms. The impact load then dropped to a value of 31 kN at 3.6 ms and fluctuated around 30 kN until t= 5 ms. The impact load increased again and fluctuated around a value of 170 kN before it dropped back to zero at the end of the impact. The inertia load coincided with the impact load during the first 5 ms of impact. This indicates that the inertia force was influenced by the drop height and stiffness of the surface of contact. The inertia load then dropped and fluctuated around 60 kN in the negative side (indicating that the acceleration took place in the opposite direction) before the inertia load returned to zero at the end of the impact. The reaction force had no contribution in the first 5 ms of the impact, as the stress waves of the impact load did not reach the supports. The reaction force started increasing at t= 5 ms. The reaction force increased to reach a maximum of 258 kN at 18 ms then dropped back to zero at the end of the impact.

It was observed that during the first 5 ms of the impact, the impact and inertia loads were not influenced by the shear capacities of the beams. Regardless of the shear capacity of the beam, the impact load started from zero and increased to the maximum at 1.7 ms then decreased back to zero. It was observed that the impact loads and impulses (area under the impact load versus time curve [44,45]) were almost similar for all beams belonging to the same group regardless of their shear capacities. Similar observations were reported in Fujikake et al. [44].

3.3. Impact loads test

Nine GFRP-UHSC beams were tested under low-velocity impact loads. The nine beams were divided into three groups. Each group contained three beams with different shear capacities. The three beams in each group had a stirrups spacing of $D/2$ (or 150 mm), $D/3$ (or 100 mm), and $D/4$ (or 75 mm). Group 1 beams were subjected to an input impact energy of 1.4E or 9.3 kJ. Therefore, the input impact velocity of Group 1 beams was chosen to be 5.5 m/s. Similarly, Group 2 and Group 3 beams were subjected to impact velocities of 6 m/s (impact energy of 1.6E) and 6.5 m/s (impact energy of 1.8E), respectively. In order to track the cracks, each crack was numbered on Figs. 7–9. It is noted that the cracks were numbered in order from the center to right and not in the order of their appearance. The failure modes of the beams are discussed in the following sections.

3.3.1. Group 1 beams

To analyze the damage mechanisms of Group 1 beams, the video recordings of each beam collected from the high-speed camera and midspan deflection histories were analyzed. Fig. 7 presents the damage progression of Beam 150-5.5, Beam 100-5.5, and Beam 75-5.5 at three time instances. The three time instances present: the effect of beam inertia resistance (at t = 1.7 ms), the maximum midspan deflection (at t = 23–25 ms), and the post-impact damage of each beam. Beam 150-5.5 with a stirrups spacing of $D/2$ (150 mm) had the maximum allowable stirrups spacing. The other two beams (Beam 100-5.5 and Beam 75-5.5) represent the beams with higher shear capacities. The input impact energy was 1.4E for Group 1 beams.

The first impact load test was carried out on Beam 150-5.5. During the first two milliseconds of the impact, when the effect of beam inertia takes place, a flexural crack was observed at the midspan of the beam (crack 1) (Fig. 7). The flexural crack propagated vertically upwards towards the impact zone. As the beam continued deflecting, additional flexural cracks (cracks 3, 5, and 6) started developing in the beam. New flexural cracks initially started propagating parallel to the other flexural cracks vertically upwards. However, these cracks started propagating towards the impact zone and transitioned into flexure-shear cracks (cracks 3, 5, and 6) as Beam 150-5.5 continued deflecting. In addition, shear cracks (cracks 2, 4, and 7) developed in the beam. At t = 24 ms, Beam 150-5.5 reached its maximum deflection and the cracks reached their maximum widths. The maximum midspan deflection of Beam 150-5.5 was 58.3 mm. The flexure-shear cracks dominated the damage response of Beam 150-5.5. As the beam rebounded to the initial position, the impactor separated from the beam and bounced a few times on it before coming to rest. This caused additional cracks in Beam 150-5.5. This also caused minor local damage at the impact zone. Also, spalling of concrete was observed for Beam 150-5.5 in the tension zone. However, the rebounding of the impactor on the beam did not have a significant impact on the failure of the beam. The residual midspan deflection (residual deflection hereafter) of the beams was defined as the permanent deflection of the beam after impact measured from the midspan of the beam. The residual deflection of Beam 150-5.5 was 13.1 mm (Table 2). The residual deflection of Beam 150-5.5 was 22.5% of the maximum midspan deflection. After Beam 150-5.5 was subjected to impact, the residual capacity of the beam (P_r) was determined. The P_r of Beam 150-5.5 was 158 kN, which was 76% of the load-carrying capacity of the control beam. Therefore, the damage of Beam 150-5.5 could be considered Severe based on the damage classification in Section 3.1.

For the second test of Group 1 beams, the shear capacity (stirrups spacing of $D/3$) was increased compared to Beam 150-5.5. The same impact test was carried out on Beam 100-5.5. During the first two milliseconds of impact, a flexural crack (crack 1) was observed at the midspan of the beam (Fig. 7). As Beam 100-5.5 continued deflecting, additional flexure-shear cracks (cracks 3–5, and 6) were observed. In addition, shear cracks (crack 2) were observed in Beam 100-5.5. The flexure-shear cracks observed in Beam 100-5.5 were very similar to the flexure-shear cracks observed in Beam 150-5.5. However, unlike Beam 150-5.5, no shear cracks were observed in Beam 100-5.5. At t = 24 ms, Beam 100-5.5 reached its maximum deflection and the cracks reached their maximum widths (Fig. 7). The maximum midspan deflection of Beam 100-5.5 was 58 mm. No local damage was observed in Beam 100-5.5 during the impact. However, after the impactor rebounded and rested on Beam 100-5.5, minor local damage was observed in the impact zone. The residual deflection of Beam 100-5.5 was 10.3 mm, which was 17.8% of the maximum midspan deflection. After testing Beam 100-5.5 under impact loads, the residual capacity of the beam was measured. The residual capacity (P_r) of Beam 100-5.5 was 168 kN, which was 81% of the load-carrying capacity of the control beam. Therefore, the damage of Beam 100-5.5 could be considered Medium.

The final impact loads test for Group 1 beams was carried out for Beam 75-5.5 (stirrups spacing of $D/4$). Beam 75-5.5 had the highest shear capacity among Group 1 beams. Similar to Beam 150-5.5 and Beam 100-5.5, a flexural crack (crack 1) was observed during the first two milliseconds of the impact (Fig. 7). As the beam continued deflecting, the flexural crack (crack 1) widened and additional flexural cracks (cracks 2 and 3) formed. In addition, flexure-shear cracks appeared in Beam 75-5.5 (cracks 4–6). The shear crack (crack 7) observed was minor in comparison to the other flexural and flexure-shear cracks. At t = 24 ms, Beam 75-5.5 reached the maximum midspan deflection of

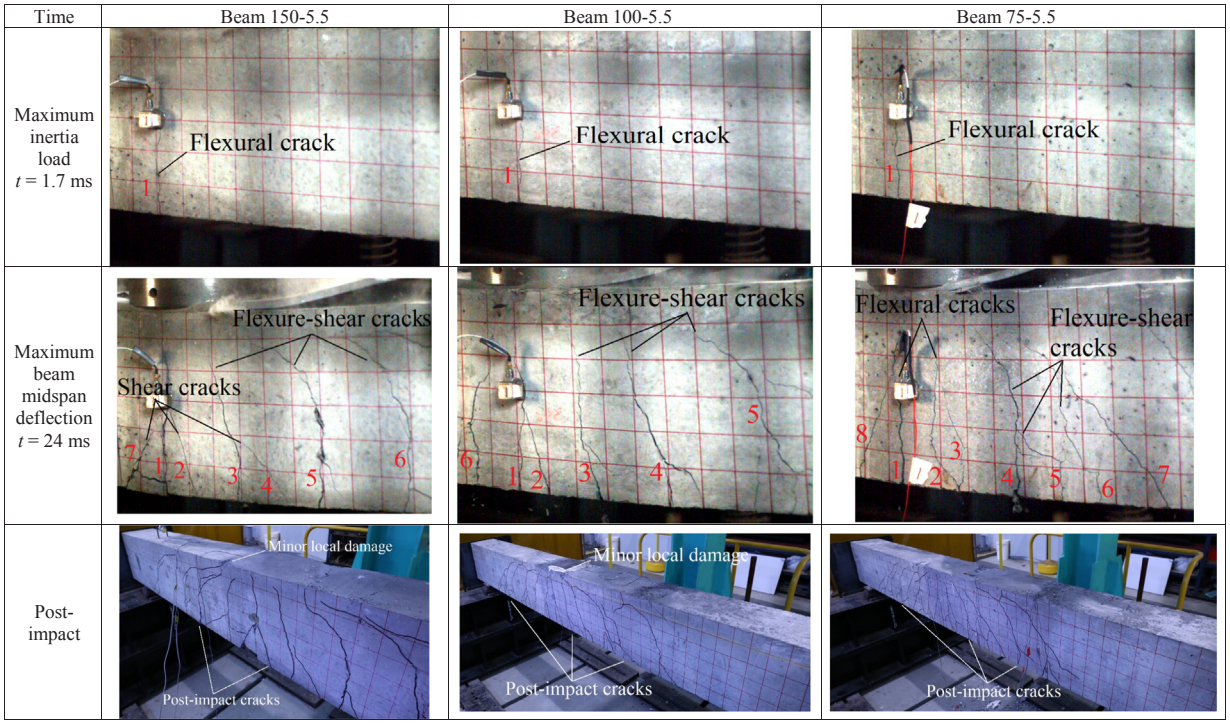

Fig. 7. Damage progression of Group 1 beams under impact loads.

57.8 mm. The flexural cracks appeared to be more dominant than the flexure-shear cracks. The higher shear capacity of Beam 75-5.5 led to a better resistance of the shear cracks and flexure-shear cracks than Beams 150-5.5 and 100-5.5. The impactor bounced off Beam 75-5.5. However, no local damage was observed for Beam 75-5.5. The residual deflection was 9.2 mm, which was 16% of the maximum midspan deflection of Beam 75-5.5. After the impact, the residual capacity of Beam 75-5.5 measured. The residual capacity (P_r) was 171 kN, which was 82% of the load-carrying capacity of the control beam. The damage of Beam 75-5.5 could be considered to be Medium. After the impact load tests, the beams of Group 1 were visually inspected and no slip between the GFRP bars and concrete was observed.

It was observed for Group 1 beams that regardless of the shear capacity of the beam, a flexural crack at the midspan of the beam developed during the beam inertia effect phase (first two milliseconds of the impact). Moreover, it was observed that beams with lower shear

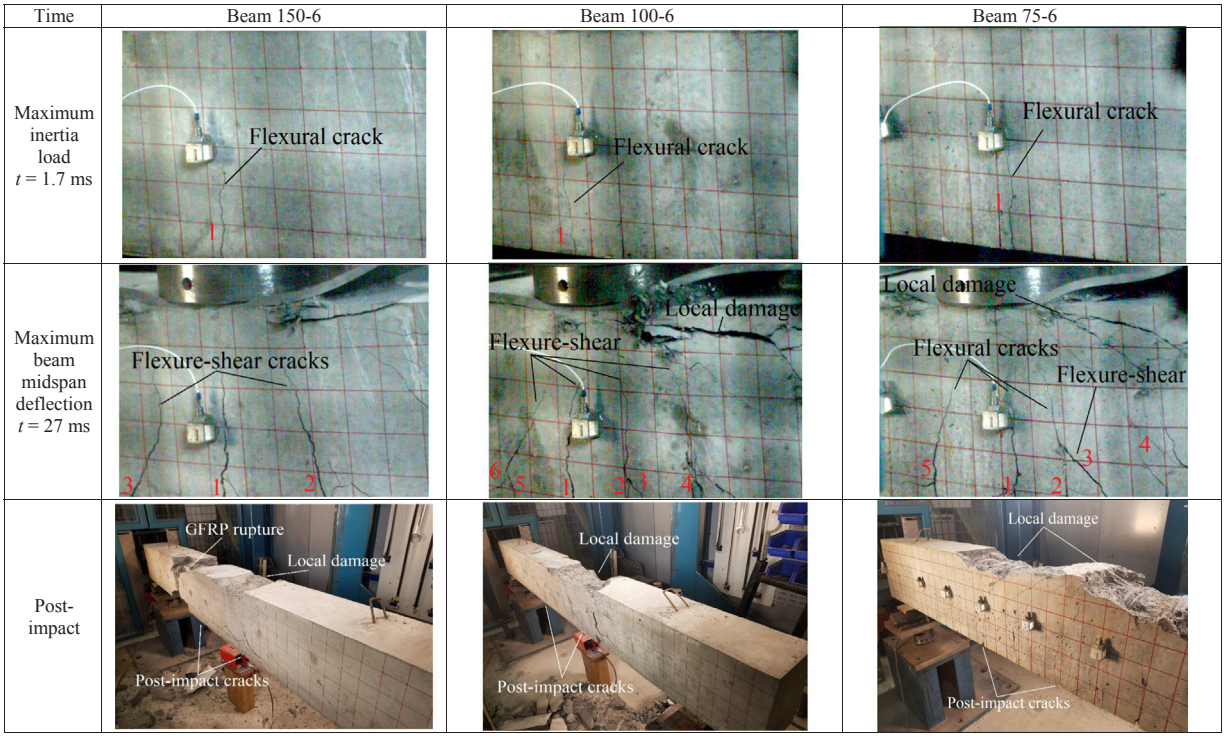

Fig. 8. Damage progression of Group 2 beams under impact loads.

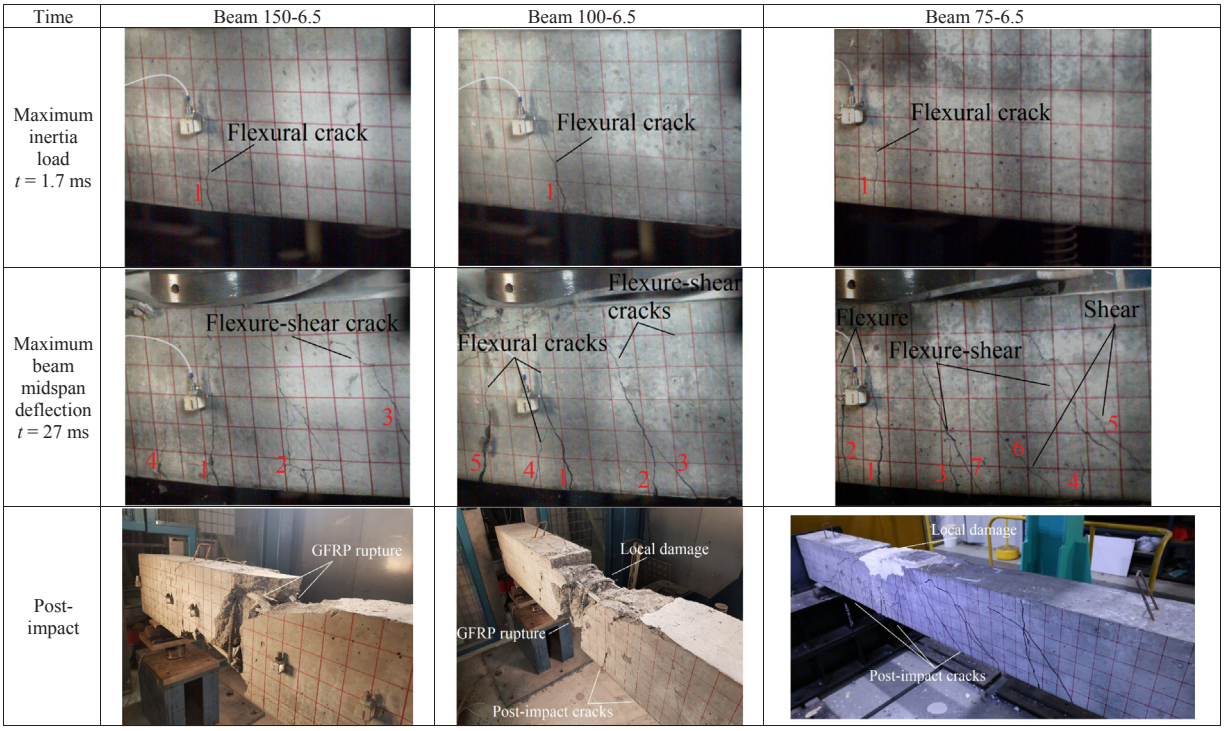

Fig. 9. Damage progression of Group 3 beams under impact loads.

capacity (Beam 150-5.5) experienced dominant shear cracks and flexure-shear cracks, whereas beams with higher shear capacity (Beam 75-5.5) experienced dominant flexural cracks. The shear capacities of the beams significantly influenced the residual deflections and residual capacities of the beams. The increase in the shear capacity led to a transformation in the damage level from severe (76% for Beam 150-5.5) to medium (82% for Beam 75-5.5). Also, the residual deflection of Beam 75-5.5 was 30% smaller than the residual deflection of Beam 150-5.5. It was also observed that the maximum midspan deflection of the beams was not influenced by their shear capacities.

3.3.2. Group 2 beams

No beams failed by GFRP bars rupture in Group 1 beams. Therefore, the impact energy was increased to assess the overloading impact damage of the beams. The impact energy for Group 2 beams was increased to 1.6*E* (10.6 kJ). The equivalent input impact velocity was 6 m/s. The first tested beam of Group 2 was Beam 150-6 (stirrups spacing of $D/2$). It was observed from Fig. 8 that during the inertia loading stage, a flexural crack (crack 1) developed at the midspan of the beam. The beam continued deflecting and dominant flexure-shear cracks (cracks 1–3) appeared in Beam 150-6. The flexure-shear cracks widened as the beam deflected and additional shear cracks developed at the impact zone propagating towards the supports. Moreover, local damage was observed in the impact zone. As Beam 150-6 continued deflecting, the GFRP bars in tension ruptured. By analyzing the midspan deflection history and the high-speed video recording of Beam 150-6, it was observed that the GFRP bars in tension partially ruptured upon Beam 150-6 reaching its maximum midspan deflection. However, the GFRP bars did not fully rupture and Beam 150-6 rebounded. Then, the impactor bounced a few times on the beam causing the GFRP bars to fully rupture. The post-impact cracks and the local damage of Beam 150-6 are presented in Fig. 8. The residual deflection and residual capacity of Beam 150-6 were not measured due to the GFRP bars rupture. Therefore, the residual capacity (P_r) of Beam 150-6 was zero and the damage could be considered Severe based on the damage classification in Section 3.1.

The shear capacity of the beam was increased for the second test of Group 2 beams. Beam 100-6 (stirrups spacing of $D/3$), similar to all the previous beams, Beam 100-6 developed a flexural crack (crack 1) during the inertia loading stage. As Beam 100-6 continued deflecting, flexure-shear cracks (cracks 3 and 4) and additional flexural cracks (crack 2) were observed. At t = 27 ms, Beam 100-6 reached its

Table 2
Midspan deflection details of the tested beams.

Beam group	Beam name	Impact velocity (m/s)	Maximum midspan deflection (mm) (Δ_{max})	Time at maximum midspan deflection (s) ($t_{\Delta_{max}}$)	Time at final position (s) (t_{final})	Residual midspan deflection (mm) (Δ_{res})
1	150-5.5	5.5	58.3	24.8	47.7	13.1
	100-5.5		58.0	24.2	46.5	10.3
	75-5.5		57.8	23.9	46.3	9.2
2	150-6	6	N/A	N/A	N/A	N/A
	100-6		75.2	27.5	60.4	16.4
	75-6		74.7	26.2	52.4	15.5
3	150-6.5	6.5	N/A	N/A	N/A	N/A
	100-6.5		N/A	N/A	N/A	N/A
	75-6.5		72.6	27.0	56.1	12.7

*Note: Δ_{max}: maximum midspan deflection, $t_{\Delta_{max}}$: time at maximum midspan deflection, t_{final}: time when the beam returned to its initial position, and Δ_{res}: residual midspan deflection.

maximum midspan deflection of 75.2 mm. Moreover, local damage was observed in the impact zone and the concrete cover in compression was damaged. The GFRP stirrups were exposed (Fig. 8). Beam 100-6, unlike Beam 150-6, did not collapse. The increase in the shear capacity of Beam 100-6 prevented the beam from severe failure. Beam 100-6 rebounded to its initial position and the residual deflection was measured as 16.4 mm, which was 22% of the maximum midspan deflection. Since the GFRP bars did not rupture, the residual capacity of Beam 100-6 was tested. The residual capacity (P_r) of Beam 100-6 was 142 kN, which was 68% of the load-carrying capacity of the control beam. Therefore, the damage of Beam 100-6 could be considered Severe.

For the last test of Group 2 beams, Beam 75-6 with a stirrups spacing of $D/4$ was tested. The same flexural crack (crack 1) was observed in all Group 1 and Group 2 beams during the first two milliseconds of impact (Fig. 8). As Beam 75-6 continued deflecting, flexure-shear cracks (cracks 2–4, and 6) were observed. Local damage was also observed in Beam 75-6 during the impact. The maximum midspan deflection measured for Beam 75-6 was 74.7 mm. The residual deflection of Beam 75-6 was 15.5 mm, which was 20.7% of the maximum midspan deflection. The residual capacity of Beam 75-6 was 166 kN. The residual capacity (P_r) of Beam 75-6 was 80% of the load-carrying capacity of the control beam. Therefore, the increase in the shear capacity from stirrups spacing of $D/3$ to $D/4$ influenced the damage levels of the beams. The damage of Beam 75-6 could be considered Medium. After the impact load tests, the beams of Group 2 were visually inspected and no slip between the GFRP bars and concrete was observed.

It was observed for Group 2 beams that the shear capacity significantly influenced that damage levels of the beams. Beams with lower shear capacity (Beam 150-6) failed by the rupture of GFRP bars. An increase in the shear capacity led to severe damage of Beam 100-6, avoiding the collapse of the beam. A further increase in the shear capacity (Beam 75-6) led to Medium damage.

3.3.3. Group 3 beams

In the tests carried out for Group 2 beams, only Beam 150-6 failed by the rupture of GFRP bars. Therefore, the input impact energy was increased to 1.8*E* (11.9 kJ) to assess the damage of the GFRP-UHSC beams under overloading impact conditions. The first beam of Group 3 beams tested was Beam 150-6.5 (stirrups spacing of $D/2$). Similar to all the other beams tested, a flexural crack (crack 1) was observed during the first two milliseconds of impact (Fig. 9). As Beam 150-6.5 continued deflecting, additional flexure-shear cracks (cracks 2 and 3) and flexural cracks (crack 4) were observed in the beam. A major shear crack was observed in Beam 150-6.5 propagating from the impact zone towards the support. The widths of the cracks increased as the beam deflected. At $t = 22$ ms, Beam 150-6.5 completely collapsed due to GFRP bars rupture. The flexure-shear cracks closed when the beam collapsed. The post-impact image of Beam 150-6.5 (Fig. 9) shows the clear failure of the beam by shear and the rupture of the GFRP bars. No local damage was observed in the impact zone as well. Since Beam 150-6.5 completely collapsed, the residual deflection and residual capacity were not measured. The damage could be considered Severe and the residual capacity was zero.

The second test was carried out for Beam 100-6.5 (stirrups spacing of $D/3$), where a flexural crack was observed during the inertia effect phase (Fig. 9). As Beam 100-6.5 continued deflecting, additional flexural cracks (cracks 4 and 5) parallel to crack 1 were observed. In addition, flexure-shear cracks (cracks 2) and shear cracks (crack 3) were observed in Beam 100-6.5 as well. Similar to Beam 150-6.5, a major shear crack appeared in the beam originating at the impact zone and propagating towards the support. At $t = 24$ ms, Beam 100-6.5 failed by the rupture of GFRP bars. The major shear crack was clearly visible in the post-impact damage image of Beam 100-6.5 (Fig. 9). The residual capacity of Beam 100-6.5 was considered to be zero and the damage was Severe.

The final beam tested was Beam 75-6.5 (stirrups spacing of $D/4$). A flexural crack (crack 1) appeared in the beam during the first two milliseconds of impact (Fig. 9). After 2 ms of impact, flexural crack 2 was observed in Beam 75-6.5. As the beam continued deflecting, flexure cracks (cracks 3 and 4) were observed in Beam 75-6.5. At $t = 13$ ms, the flexural cracks (cracks 1 and 2) and the flexure-shear cracks (cracks 3 and 4) were the dominant cracks in Beam 75-6.5. As the beam continued deflecting, the shear cracks (cracks 5–7) were observed in the beam and merged with the flexure-shear cracks. At $t = 27$ ms, Beam 75-6.5 reached its maximum midspan deflection and the cracks reached their maximum widths. The beam then rebounded to its initial position and the impactor caused local damage at the impact zone. The maximum midspan deflection and residual deflection of Beam 75-6.5 were 72.6 mm and 12.7 mm, respectively. The residual deflection was 17.5% of the maximum midspan deflection. The residual capacity (P_r) of Beam 75-6.5 was 157 kN, which was 75% of the load-carrying capacity of the control beam. Thus, the damage of Beam 75-6.5 could be considered Severe. After the impact load tests, the beams of Group 3 were visually inspected and no slip between the GFRP bars and concrete was observed.

It was observed that beams with lower shear capacities (Beam 150-6.5 and Beam 100-6.5) failed catastrophically by GFRP bars rupture under impact loads. However, Beam 75-6.5 (stirrups spacing of $D/4$), with higher shear capacity, had some residual capacity. It was also observed that beams with lower shear reinforcement failed due to a major shear crack.

4. Discussion of the damage mechanisms of GFRP-UHSC under impact overloads

In this study, three stirrup spacings were chosen for the nine tested beams. The stirrup spacings were 150 mm or $D/2$, 100 mm or $D/3$, and 75 mm or $D/4$. To assess the damage of GFRP-UHSC beams under overloading impact conditions, three input impact energies were used. The input impact energies were 9.3 kJ, 10.6 kJ, and 11.9 kJ which correspond to 1.4*E*, 1.6*E*, and 1.8*E*, respectively. Fig. 10 presents the damage matrix of GFRP-UHSC beams with three shear capacities (stirrups spacing of $D/2$, $D/3$, or $D/4$) under variable impact energies (1.4*E*, 1.6*E*, or 1.8*E*). It was observed that under an input impact energy of 1.4*E*, Beam 150-5.5 (stirrups spacing of $D/2$,) and Beam 100-5.5 (stirrups spacing of $D/3$,) failed in the flexure-shear mode, whereas Beam 75-5.5 (stirrups spacing of $D/4$,) failed in the flexure mode. No beams failed in shear and all three beams had some residual capacities. When the input impact energy was increased to 1.6*E*, Beam 100-6 and Beam 75-6 of Group 2 failed in the flexure-shear mode. Both beams were able to resist the impact loads and had some residual capacities. However, Beam 150-6, failed in the shear mode and the GFRP bars ruptured. The residual capacity of Beam 150-6 was zero. The input impact load was further increased to 1.8*E* and Group 3 beams were

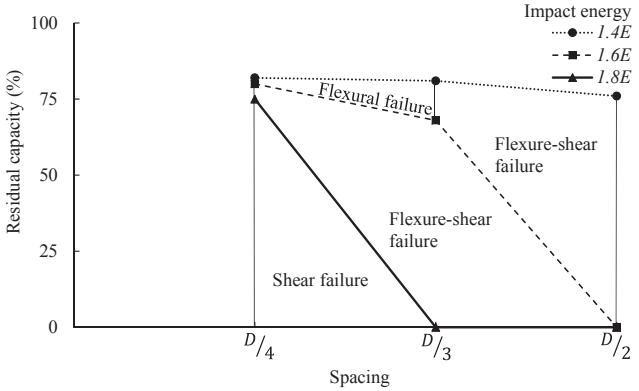

Fig. 10. Failure mode diagram of GFRP-UHSC beams with different shear capacities under variable impact energies.

tested. Beam 100-6.5 and Beam 150-6.5 both failed in the shear mode and the rupture of the GFRP bars in tension and compression was observed. The residual capacity of both beams was zero. On the other hand, Beam 75-6.5 failed in the flexure-shear mode without the rupture of the GFRP bars.

Therefore, it can be concluded that for input the impact energy up to 1.4*E*, GFRP-UHSC beams can resist the impact loads regardless of the shear capacity of the beam. For input impact energies between 1.4*E* and 1.6*E*, only beams with higher shear capacities (stirrups spacing of $D/3$ or $D/4$) were able to resist the impact loads and had residual capacities. Moreover, for input impact energies between 1.6*E* and 1.8*E*, only beams with high shear capacities (i.e. Beam 75-6.5) were able to resist the impact loads. For input impact energies higher than 1.8*E*, additional experiments must be carried out to determine the input impact failure energy for beams with high shear capacities.

5. Design recommendations

5.1. Verification of observed failure modes

For beams under quasi-static loads, the ACI [27] did not specify an upper limit for the compressive strength of concrete beyond which the equations for shear design are not applicable. Therefore, the shear capacities of the GFRP-UHSC beams were calculated according to ACI [27]. The nominal shear strength (V_n), presented in Eq. (2), is the sum of the shear resistance provided by the GFRP shear reinforcement (V_f) and the nominal shear strength provided by concrete (V_c). The shear capacities for the nine GFRP-UHSC beams were presented in Table 3.

$$V_n = V_f + V_c \tag{2}$$

The resistance provided by the GFRP shear reinforcement is calculated by Eq. (3) (SI units)

$$V_s = \frac{A_f f_f d}{s} \tag{3}$$

where f_f is the tensile strength of the shear reinforcement (in MPa), s is the center-to-center spacing of the shear reinforcement (in mm), and A_f (in mm^2) is the area of the shear reinforcement in the spacing s.

The nominal shear strength provided by concrete is calculated by Eq. (4)

$$V_c = \frac{2}{5}\sqrt{f_c'}\, b(kd) \tag{4}$$

where f_c' is the compressive strength of concrete (in MPa), b is the width of the beam (in mm), k is the ratio of depth of neutral axis to reinforcement depth (Eq. (5)), and d is the distance from extreme compression fiber to centroid of tensile longitudinal bars (in mm).

$$k = \sqrt{2\rho_f n_f + (\rho_f n_f)^2} - \rho_f n_f \tag{5}$$

where ρ_f is the longitudinal reinforcement ratio and n_f is the modular ratio calculated by Eq. (6)

$$n_f = \frac{E_f}{E_c} \tag{6}$$

where E_f is the modulus of elasticity of the GFRP bars and E_c is the modulus of elasticity of concrete (calculated as $4700\sqrt{f_c'}$ for f_c' in MPa).

Table 3 presents the results of the experimental maximum dynamic shear forces (V_e), nominal shear capacities (V_n) calculated according to ACI [27], and the failure modes for the nine GFRP-UHSC beams. The nominal shear capacities of the beams with a stirrup spacing of 75 mm, 100 mm, and 150 mm were 378 kN, 290 kN, and 202 kN, respectively. Moreover, the experimental maximum dynamic shear force was derived for each of the nine tested beams using the recordings from the accelerometers mounted along the beams. The experimental maximum dynamic shear force (V_e) was compared to the nominal shear capacity (V_n). If the experimental maximum shear force was smaller than the nominal shear capacity ($V_e < V_n$), the failure mode was considered to be flexural failure. If the experimental maximum shear force was approximately equal to the nominal shear capacity ($V_e \approx V_n$), then the failure mode was considered to be flexure-shear. If the experimental maximum shear force was larger than the nominal shear capacity ($V_e > V_n$), the failure mode was considered to be a shear failure. The theoretical calculations were carried out in this section to verify the observations of Section 3.3. The failure modes observed for all beams were in agreement with the predicted failure modes.

5.2. Effect of stirrup spacing on failure modes

The shear capacities of the GFRP-UHSC beams subjected to impact loading influenced their failure modes, residual capacities, and residual deflections. In terms of the failure modes, it was observed that the three beams with higher shear capacities (Beam 75-5.5, Beam 75-6, and Beam 75-6.5 with a stirrup spacing of $D/4$) failed in flexure or flexure-shear modes for the full range of the input impact energies considered in this study. However, when the shear capacity of the beams decreased (Beam 150-5.5, Beam 150-6, and Beam 150-6.5 with a stirrup spacing of $D/2$), the beams failed in flexure-shear and shear modes. The higher shear capacities of the beams resisted the development and propagation of dominant shear cracks during the impact.

In terms of the residual capacities of the beams, it was observed that beams with higher shear capacities had higher post-impact residual capacities. Beams 75-5.5, 75-6, and 75-6.5 (stirrup spacing of $D/4$) had residual capacities of 82%, 80%, and 75% of the load-carrying capacities, respectively. Moreover, Beams 100-5.5, 100-6, and 100-6.5 (stirrup spacing of $D/3$) had residual capacities of 81%, 68%, and 0% of the load-carrying capactieis, respectively. It was observed that under the same input impact energy, beams with higher shear capacities had higher residual capacities. Similarly, under the same input impact

Table 3
Shear capacities of the tested beams.

Beam group	Beam name	Experimental maximum shear force (V_e)(kN)	Shear capacity according to ACI [27] (V_n)(kN)	Residual load-carrying capacity (P_r)(kN)	Ratio of residual capacity to control beam load-carrying capacity $\left(\frac{P_r}{P}\right)$	Failure mode
1	150-5.5	210	202	158	0.76	Flexure-shear
	100-5.5	212	290	168	0.81	Flexure-shear
	75-5.5	211	378	171	0.82	Flexural
2	150-6	300	202	0	0	Shear
	100-6	297	290	142	0.68	Flexure-shear
	75-6	303	378	166	0.80	Flexure-shear
3	150-6.5	387	202	0	0	Shear
	100-6.5	391	290	0	0	Shear
	75-6.5	392	378	157	0.75	Flexure-shear

*Note: V_e: experimental maximum shear force, V_n: shear capacity according to ACI [27], P_r: residual load-carrying capacity, and P: load-carrying capacity of control beam.

energy, beams with a stirrup spacing of $D/3$ had higher residual capacities than beams with a stirrup spacing of $D/2$. The same effect was observed for the residual deflections of the beams. Under the same input impact energy, beams with a stirrup spacing of $D/4$ had lower residual deflections than beams with stirrup spacing of $D/3$ and $D/4$.

Therefore, for an input impact energy up to 1.4E, the maximum allowed stirrup spacing ($D/2$) was sufficient to resist the impact and to achieve a residual capacity up to 76% of the load-carrying capacity. It is noted, however, that an increase in the shear capacity from that recommended in ACI [27] and CSA [28] (from $D/2$ to $D/3$ or $D/4$) is advised to avoid shear mode failure under low-velocity impact load. Moreover, an increase in the shear capacity is also recommended to achieve medium damage (Section 3.1) and residual capacities up to 80% of the load-carrying capacity.

For an input impact energy between 1.4E and 1.6E, an increase in the shear capacity (from $D/2$ to $D/2$ or $D/4$) of the beam is required for the beam to resist the impact loads, avoid shear mode failure, and have residual capacity up to 68% of the load-carrying capacity. It is noted that for an input impact energy between 1.4E and 1.6E, an increase in the shear capacity (stirrup spacing of $D/4$) is recommended for the beam to have medium damage and a residual capacity up to 80% of the load-carrying capacity.

For an input impact energy higher than 1.6E, an increase in the shear capacity (from $D/2$ and $D/3$ to $D/4$) is recommended for the beam to avoid catastrophic failure and to achieve residual capacity up to 75% of the load-carrying capacity. However, the damage of the beam was still considered severe and a further increase in the shear capacity is required for the beam to achieve a higher residual capacity.

5.3. Effect of the variability of the compressive strength of concrete on failure modes

The nominal shear strength provided by concrete was discussed in Section 5.1. Increasing the compressive strength of concrete increases the nominal shear strength provided by concrete. For example, in the case of the beams tested in this study, had the target compressive strength of concrete of 80 MPa been achieved, then the nominal shear strength provided by concrete (V_c) would have been equal to 22 kN. Since the compressive strength of concrete increases with time, the achieved compressive strength of concrete was 118 MPa. Hence, the nominal shear strength provided by concrete (V_c) became 24.3 kN. The 11% increase in the nominal shear strength (between 80 MPa and 118 MPa) provided additional resistance to the shear cracking under impact loads. The nominal section shear capacity (V_n) was between 202 kN and 378 kN (Table 3), depending on the stirrup spacing used. Therefore, the contribution of V_c to V_n was between 6% and 12% and the increase in the compressive strength of concrete had a minor effect on the total shear capacity (V_n) of the section. However, the increase in the compressive strength of concrete had a significant influence on the ratio of reinforcement (ρ/ρ_b) of the beam. According to ACI [27], to determine whether a GFRP-UHSC beam is under-reinforced, balanced, or over-reinforced, the reinforcement ratio of the beam (ρ) is divided by the balanced reinforcement ratio (ρ_b) of the beam. If the ratio ρ/ρ_b is under 1, the beam is under-reinforced. If the ratio ρ/ρ_b is between 1 and 1.4, the beam is balanced. If the ratio ρ/ρ_b is over 1.4, the beam is over-reinforced. Had the target compressive strength of concrete of 80 MPa been achieved, then ρ/ρ_b would have been equal to 1.43, meaning the beams would have been at a borderline between balanced and over-reinforced designs. However, the ratio ρ/ρ_b equals 0.97 for the compressive strength of concrete of 118 MPa, meaning that the expected performance of the beam has shifted from over-reinforced design to under-reinforced design. Therefore, since the compressive strength of concrete increases with time, it is recommended to design the GFRP-UHSC beams with a sufficient margin of safety over the ratio ρ/ρ_b to avoid the transition in the failure modes of the beams from more ductile over-reinforced design to brittle under-reinforced and balanced modes of failure. Based on the results of this study, it is recommended to design GFRP-UHSC beams with a factor of safety that prevents the transition in the failure modes (from concrete crushing to FRP bar rupture) of the beams from happening. Based on the results of this study, the ρ/ρ_b ratio of larger than 2 is recommended to avoid the transition in the failure mode due to the increase in the compressive strength of concrete.

The reinforcement of the beams in this study comprised two 16 mm diameter GFRP bars in tension. If the beams had been designed with three 16 mm diameter GFRP bars in tension (assuming 80 MPa concrete strength), the ratio of reinforcement ρ/ρ_b would have been $2.04 > 2.0$. This would have prevented some beams in this study from transitioning from an over-reinforced design to an under-reinforced design as the compressive strength of concrete increased over time. It is noted that for the actual concrete strength of 118 MPa in this study, the beam designs with three 16 mm bars in tension would have produced the reinforcement ratio ρ/ρ_b of $1.44 > 1.4$, which is an over-reinforced design of the beam.

6. Conclusions

In this paper, the damage assessment of GFRP-UHSC beams under overloading impact conditions was carried out by conducting a series of impact load tests. The Impact load tests were carried out on nine GFRP-USCHC beams to investigate the influence of the shear capacity and input impact energy on the behavior of GFRP-UHSC under overloading impact conditions. The overloading impact condition is defined as the input impact energy larger than the quasi-static energy absorption capacity of the beam. Also, the residual capacities of the beams were measured to determine the level of the damage. Based on the results of the experimental investigations, the following conclusions are drawn:

1. The shear capacities of the GFRP-UHSC beams significantly influenced the failure modes of the beams under overloading impact conditions. Beams with higher shear capacities failed in flexure and flexure-shear modes, whereas beams with lower shear capacities failed in dominant shear and flexure-shear modes under similar impact loading conditions.
2. It was observed that, under input impact energies higher than the quasi-static energy absorption capacity (E) of a beam, increasing the shear capacities of the beams from that recommended in ACI [27] was necessary to resist brittle failure. For input impact energies up to 1.4E, a stirrup spacing of $D/2$ (D is the beam depth) is required to resist the overloading impact conditions. For input impact energies between 1.4E and 1.6E, a stirrup spacing of $D/3$ is required for the beam to avoid catastrophic failure and resist the overloading impact conditions. Moreover, for input impact energies higher than 1.6E, a stirrup spacing of $D/4$ is required for the beam to resist the overloading impact conditions.
3. Based on the experimental observations, a damage classification system depending on the residual capacities of the GFRP-UHSC beams was introduced. If the residual capacity was higher than 90% of the load-carrying capacity, the damage was considered Minor. If the residual capacity was between 80% and 90% of the load-carrying capacity, the damage was considered Medium. If the residual capacity was lower than 80% of the load-carrying capacity, the damage was considered Severe.
4. The transition in failure modes from initially designed over-reinforced to balanced or under-reinforced may occur due to the increase in compressive strength of concrete over time for beams designed with the ratio ρ/ρ_b just over 1.4, as per code recommendations in ACI [27]. Therefore, it is recommended to design GFRP-UHSC beams with the ratio ρ/ρ_b larger than 2 to avoid the shift from quasi-ductile to brittle failure modes due to variations in concrete strength.

The experiments carried out in this paper were limited to a fixed shear span-to-effective depth ratio. The shear span-to-effective depth ratio may have an influence on the impact resistance of GFRP-RC beams, which needs to be investigated adequately. Also, GFRP-USHC beams need to be numerically modelled to investigate the influence of different parameters on the behavior of GFRP-UHSC beams under overloading impact conditions.

CRediT authorship contribution statement

Zein Saleh: Investigation, Writing - original draft, Visualization, Validation. **M. Neaz Sheikh:** Conceptualization, Methodology, Resources, Supervision, Writing - review & editing. **Alex Remennikov:** Conceptualization, Methodology, Resources, Supervision, Writing - review & editing. **Abheek Basu:** Supervision, Writing - review & editing.

Declaration of Competing Interest

None.

Acknowledgments

The authors express their gratitude to the University of Wollongong for providing the funding and facilities for the experimental work. The authors thank the technical officers for their contributions in the experiments. The authors also express their appreciation to Ian Cumming (Director IRC Pty Ltd) and Pultron (www.pultron.com) for providing the GFRP bars used in the experimental program.

References

[1] Adam MA, Said M, Mahmoud AA, Shanour AS. Analytical and experimental flexural behavior of concrete beams reinforced with glass fiber reinforced polymers bars. Constr Build Mater 2015;84:354–66.
[2] Alsayed SH. Flexural behaviour of concrete beams reinforced with GFRP bars. Cem Concr Compos 1998;20:1–11.
[3] Ashour AF. Flexural and shear capacities of concrete beams reinforced with GFRP bars. Constr Build Mater 2006;20:1005–15.
[4] Barris C, Torres L, Turon A, Baena M, Catalan A. An experimental study of the flexural behaviour of GFRP RC beams and comparison with prediction models. Compos Struct 2009;91:286–95.
[5] El-Mogy M, El-Ragaby A, El-Salakawy E. Effect of transverse reinforcement on the flexural behavior of continuous concrete beams reinforced with FRP. J Compos Constr 2011;15:672–81.
[6] El-Nemr A, Ahmed EA, Benmokrane B. Flexural behavior and serviceability of normal- and high-strength concrete beams reinforced with glass fiber-reinforced polymer bars. ACI Struct J 2013;110:1077–87.
[7] Kalpana VG, Subramanian K. Behavior of concrete beams reinforced with GFRP BARS. J Reinf Plast Compos 2011;30:1915–22.
[8] Karim H, Sheikh MN, Hadi MNS. Longitudinal reinforcement limits for fiber-reinforced polymer reinforced concrete members. ACI Struct J 2017;114:687–96.
[9] Saleh Z, Sheikh MN, Remennikov AM, Basu A. Numerical investigations on the flexural behavior of GFRP-RC beams under monotonic loads. Structures 2019;20:255–67.
[10] Goldston M, Remennikov A, Sheikh MN. Experimental investigation of the behaviour of concrete beams reinforced with GFRP bars under static and impact loading. Eng Struct 2016;113:220–32.
[11] Wang W, Sheikh MN, Hadi MN, Gao D, Chen G. Behaviour of concrete-encased concrete-filled FRP tube (CCFT) columns under axial compression. Eng Struct 2017;147:256–68.
[12] Saleh Z, Goldston M, Remennikov AM, Sheikh MN. Flexural design of GFRP bar reinforced concrete beams: an appraisal of code recommendations. J Build Eng 2019:100794.
[13] El-Nemr A, Ahmed EA, El-Safty A, Benmokrane B. Evaluation of the flexural strength and serviceability of concrete beams reinforced with different types of GFRP bars. Eng Struct 2018;173:606–19.
[14] Focacci F, Nanni A, Bakis CE. Local bond-slip relationship for FRP reinforcement in concrete. J Compos Constr 2000;4:24–31.
[15] Gravina RJ, Smith ST. Flexural behaviour of indeterminate concrete beams reinforced with FRP bars. Eng Struct 2008;30:2370–80.
[16] Fang Z, Zhang K, Tu B. Experimental investigation of a bond-type anchorage system for multiple FRP tendons. Eng Struct 2013;57:364–73.
[17] Benmokrane B, Chaallal O, Masmoudi R. Glass fibre reinforced plastic (GFRP) rebars for concrete structures. Constr Build Mater 1995;9:353–64.
[18] Rolland A, Quiertant M, Khadour A, Chataigner S, Benzarti K, Argoul P. Experimental investigations on the bond behavior between concrete and FRP reinforcing bars. Constr Build Mater 2018;173:136–48.
[19] Smith ST, Teng JG. FRP-strengthened RC beams. I: review of debonding strength models. Eng Struct 2002;24:385–95.
[20] Smith ST, Teng JG. FRP-strengthened RC beams. II: assessment of debonding strength models. Eng Struct 2002;24:397–417.
[21] Theriault M, Benmokrane B. Effects of FRP reinforcement ratio and concrete strength on flexural behavior of concrete beams. J Compos Constr 1998;2:7–16.
[22] Vincent T, Ozbakkaloglu T. Influence of concrete strength and confinement method on axial compressive behavior of FRP confined high-and ultra high-strength concrete. Composites Part B: Eng 2013;50:413–28.
[23] Faza S, GangaRao H. Glass FRP reinforcing bars for concrete. Fiber reinforced (FRP) reinforcement for concrete structures: properties and applications In: Developments in civil engineering. 1993;42:167–88.
[24] Nanni A. Flexural behavior and design of RC members using FRP reinforcement. J Struct Eng 1993;119:3344–59.
[25] Yost JR, Gross SP. Flexural design methodology for concrete beams reinforced with fiber-reinforced polymers. Struct J 2002;99:308–16.
[26] Idris Y, Ozbakkaloglu T. Flexural behavior of FRP-HSC-steel composite beams. Thin-Wall Struct 2014;80:207–16.
[27] ACI. Guide for the Design and Construction of Structural Concrete Reinforced with Fiber-Reinforced Polymer (FRP) Bars (ACI 440.1R-15). American Concrete Institute, Farmington Hills, MI 48331; 2015.
[28] CSA. Design and construction of building structures with fibre-reinforced polymers: Canadian Standards Association; 2012.
[29] Cladera A, Mari A. Experimental study on high-strength concrete beams failing in shear. Eng Struct 2005;27:1519–27.
[30] El-Sayed AK, El-Salakawy EF, Benmokrane B. Shear capacity of high-strength concrete beams reinforced with FRP bars. ACI Struct J 2006;103:383.
[31] Johnson MK, Ramirez JA. Minimum shear reinforcement in beams with higher strength concrete. Struct J 1989;86:376–82.
[32] Pendyala RS, Mendis P. Experimental study on shear strength of high-strength concrete beams. Struct J 2000;97:564–71.
[33] Yoon YS, Cook WD, Mitchell D. Minimum shear reinforcement in normal, medium, and high-strength concrete beams. ACI Struct J 1996;93:576–84.
[34] Hughes B, AI-Dafiry H. Impact energy absorption at contact zone and supports of reinforced plain and fibrous concrete beams. Constr Build Mater 1995;9:239–44.
[35] Pham TM, Hao H. Impact Behavior of FRP-Strengthened RC Beams without Stirrups. J Compos Constr. 2016;20:04016011.
[36] Pham TM, Hao H. Review of concrete structures strengthened with FRP against impact loading. Structures 2016;7:59–70.
[37] Goldston M, Remennikov A, Sheikh MN. Flexural behaviour of GFRP reinforced high strength and ultra high strength concrete beams. Constr Build Mater 2017;131:606–17.
[38] Goldston M, Remennikov A, Saleh Z, Sheikh MN. Experimental investigations on the behavior of GFRP bar reinforced HSC and UHSC beams under static and impact loading. structures. Elsevier; 2019. p. 109–23.
[39] Saleh Z, Sheikh MN, Remennikov A, Basu A. Numerical analysis of behavior of glass fiber-reinforced polymer bar-reinforced concrete beams under impact loads. ACI Struct J 2019;116:151–60.
[40] Saleh Z, Sheikh MN, Remennikov A, Basu A. Overload damage mechanisms of GFRP-RC beams subjected to high-intensity low-velocity impact loads. Compos Struct 2020;233:111578.
[41] Adhikary SD, Li B, Fujikake K. Dynamic behavior of reinforced concrete beams under varying rates of concentrated loading. Int J Impact Eng 2012;47:24–38.
[42] Adhikary SD, Li B, Fujikake K. Residual resistance of impact-damaged reinforced concrete beams. 2014.
[43] Saatci S, Vecchio FJ. Effects of shear mechanisms on impact behavior of reinforced concrete beams. ACI Struct J 2009;106:78–86.
[44] Fujikake K, Li B, Soeun S. Impact response of reinforced concrete beam and its analytical evaluation. J Struct Eng 2009;135:938–50.
[45] Tachibana S, Masuya H, Nakamura S. Performance based design of reinforced concrete beams under impact. Nat Hazards Earth Syst Sci 2010;10:1069–78.